Annealing Time Dependence in the Fabrication of Bismuth-based Perovskite Solar Cells (Bi-PeSCs) by the Hot Immersion Method

*M. F. Achoi**
Faculty of Applied Sciences, Universiti Teknologi MARA (UiTM), Sabah Branch, Kota Kinabalu Campus, Sabah 88997, MALAYSIA
**mohdf484@uitm.edu.my*

S. Kato, N. Kishi, T. Soga
Department of Electrical and Mechanical Engineering, Nagoya Institute of Technology, Showa-ku, Gokiso-cho, Nagoya 466-8555, JAPAN

ABSTRACT

Lead-free perovskite solar cells have attracted attention as an environmentally friendly future energy source. However, their performance is still low at present due to the poor morphology of the film and the complicated process of fabrication. The annealing period, as a key parameter, has been identified to control the morphology of $MA_3Bi_2I_9$ (MBI) perovskite film fabricated by the Hot Immersion Method (HIM) with the annealing period varying between 5 to 25 minutes. SEM images visually depicted that a longer period of annealing induced perovskite film to form a larger crystallite size with a compact film, resulting in a rougher surface. The MBI films fabricated at 25 minutes showed a high crystallinity of films and exhibited a high absorption with a longer absorption wavelength and a narrow bandgap, leading to enhanced solar cell performance. By optimizing the annealing time, the efficiency of the device has been enhanced almost eight times compared to a shorter period of annealing. Our findings suggest that the compact MBI films can be obtained by using this simple method (HIM), and yet the performance of solar cell devices can be achieved, thus providing another alternative way to fabricate MBI-based perovskite solar cells (PeSC's) in the future.

Keywords: *MBI; Perovskite; Solar Cells; Hot Immersion*

ISSN 1823-5514, eISSN 2550-164X

https://doi.org/10.24191/jmeche.v21i1.25361

Received for review: 2023-01-05
Accepted for publication: 2023-07-18
Published: 2024-01-15

Introduction

Recent development in the lead (Pb)-free Perovskite Solar Cells (PeSCs) has been actively studied by previous researchers [1]-[5]. Among lots of Pb-free perovskite materials, Methylammonium Bismuth Iodide (MBI) has excellent stability [6] and is a non-toxic material [7] compared to Pb-based PeSCs [8]. Pb-based perovskite solar cells have been reported for practical use of solar cell by Roslton et al. [9]; however, studies reported on the mechanical properties of Pb-free perovskite solar cells are very few [10]. However, to date, the poor morphology and low efficiency have limited their commercialization. The highest efficiency that has ever been recorded for Bi-PeSCs is 3.17% [11], with other efficiencies recorded as 0.016% [4], 0.034% [12], 0.010% [5], etc. Moreover, poor morphology is identified as one of the factors which contribute to the low performance of Bi-PeSCs. The criteria of a good quality film include characteristics such as compactness, pinhole-free, good crystallinity, and defect free [1], [13]-[16]. Therefore, much effort is required to improve the morphology of MBI-based PeSCs by annealing [2], [15].

Annealing is an important parameter that is attributed to the quality of a film morphology. The annealing effect also might contribute to other effects such as surface morphology (uniformity and surface roughness), crystallinity, crystallite size, and the thickness of a film. All these effects might influence the solar cell device performance. For example, Chen et al. [16] reported that the larger grain sizes resulting from annealing showed stronger light absorption and thus influenced device performance. Shargaieva et al. [17] reported that an improved morphology with increasing grain size caused by the annealing led to a drastic increase in the device performance. In addition, Jiajiu et al. [18] reported that the annealing temperature affected the crystallization and morphology of the perovskite films. Moreover, Im et al. [19] and Xiao et al. [20] reported that large grain size resulting from reaction temperature is attributed to better charge transport due to fewer crystal boundaries and weaker carrier transport scattering. All these studies elucidate that annealing is a key parameter to achieving better morphology and improved crystallinity, which contributed to a better performance of Bi-PeSCs.

Previous studies on improving morphology and crystallinity discussed techniques, including spin-coating [21], spray coating [22], thermal evaporation [23], vacuum-assisted thermal annealing [24], two-step thermal annealing [25], hot casting technique [26] and low-pressure vapor annealing process [1]. Although these methods of fabrication and their results showed improvements in terms of morphology and performance of solar cells, it is difficult to effectively achieve compact, uniform films by these approaches. Furthermore, high quality perovskite films often require complicated process conditions, such as using antisolvent [27], vaporization process [1], two-step method [28], and addition of an additive to enhance crystallization [29]. Therefore, developing a simple and effective method for achieving improved

morphology and enhanced crystallization of perovskite films is highly demanded.

In this connection, the hot immersion method (HIM) was employed to fabricate MBI as reported previously [30]. In brief, HIM is a simple and effective method without employing the use of an antisolvent for the fabrication of Bi-PeSCs. This method is well-proven to fabricate a compact film and a promising method to enhance the crystallinity of MBI. It has been consistent in obtaining compact surface and pinhole-free MBI films according to our previously reported work [31]-[32]. Herein, this method is employed to evaluate the effect of the annealing period on the performance of MBI solar cell devices for the first time, with the objective of further improving the morphology and enhancing the crystallinity, and the performance of the MBI solar cells from our previously reported work [33]. To the best of our knowledge, the effect of annealing time on the morphology, crystallinity, and optical properties of MBI films has not been reported elsewhere. By optimizing the annealing reaction time, MBI films with high crystallinity and compactness can be successfully obtained and maintained. As a result, it is expected to improve the charge extraction and transport on the absorber active layer and enhance the MBI solar cell's performance, through which the performance of the device is also attainable. According to the results of this study, the solar cell parameters were improved as compared to our previously reported work [34].

Methodology

Preparation of MBI, substrate, ETL and HTL

The substrate of Fluorine Tin Oxide (FTO) glass with a dimension of 2 x 2 cm was selected as an electrode substrate. The FTO glass was cleaned with acetone and ethanol, respectively, and then dried under N_2 gas blowing [32]. Each cleaning stage was repeated two times to ensure the cleanliness of the substrate. As a next step, compact titanium dioxide/mesoporous titanium dioxide (c-TiO_2/mp-TiO_2) as an Electron Transport Layer (ETL), was prepared, and its fabrication process has already been discussed in our previously reported work [30]. In brief, both precursors of bismuth triiodide (BiI_3) and Methylammonium Iodide (MAI) were mixed in 10 mL of Dimethylformamide [$HCON(CH_3)_2$] (DMF) to form a 0.5M MBI solution. The TiO_2 coated FTO glass was immersed in the MBI solution for 24 h at 70 °C. Then, the annealing process was performed at 100 °C by changing the period from 5 min to 25 min. Finally, the preparation of poly(3-hexylthiophene-2,5-diyl) (P3HT) as a hole transport layer (HTL) was followed as reported earlier [12]. Finally, P3HT was dissolved in dichlorobenzene to make 15 $mg.mL^{-1}$ of P3HT. All this process was carried out in the glove box.

Fabrication of MBI solar cell device

All the prepared solutions in the previous step were used for the fabrication process, which was performed in the glove box. All the details of the fabrication of each layer, except for MBI, have been reported in our previous work [12], [35]. In brief, all the layers were fabricated according to the specified method as shown in Figure 1.

In the final step of preparing the MBI cells, an insulator tape (Nichiban polymer) was punched to make a hole by a puncher and displayed on top of the HTL layer (P3HT) carefully using a forceps. The punched hole size was 3 mm in the middle of the tape (hole for the carbon and silver paste), as shown in Figure 1. The active area was around 0.071 cm^2 and on this area, the graphite solution was deposited by spin coating at 5000 rpm for 20 sec, which was prepared by diluting 0.1 g of colloidal graphite in 1.5 mL of 2-propanol (0.1 g: 1.5 mL). Then, the colloidal graphite (carbon) was dried at room temperature for 5 min. The purpose of using the carbon was to provide a better connection between the connector (Ag paste) and the entire MBI cell structure [33] as shown in Figure 1. Finally, the Ag paste was put in a small amount by using a dropper on the carbon electrode. All this process was done outside of the glove box.

The characterization of MBI

The structural, morphology, and thickness of MBI films were characterized by X-ray diffraction (XRD; Rigaku RINT-2100 diffractometer) and scanning electron microscopy (SEM; JEOL JSM 7600F). For the XRD, the X-ray radiation source of Ni-filtered Cu Kα radiation with wavelength, λ = 1.5408 Å and equipped with a Cu target was used (Rigaku Smartlab). The UV-absorption properties and the surface roughness were characterized using a UV-vis spectrophotometer (JASCO ModelV-570) and the Dektak machine (Veeco-Dektak 150), respectively.

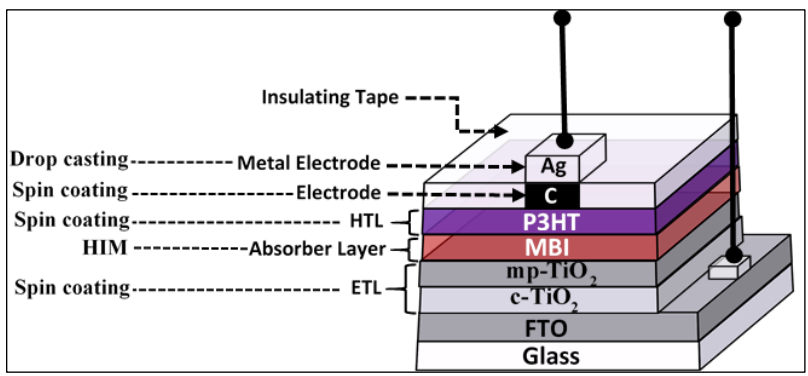

Figure 1: Structure of the MBI solar cell device

The MBI solar cell measurement

The MBI Cells were evaluated by the current-voltage measurement under a solar simulator equipped with a Xenon lamp (model PS-X500) and measured by using a 238 Keithley high current source. In addition, the simulator was configured with white light illumination at AM 1.5 and 100 $mW.cm^{-2}$ of class AA spectra. The voltage interval used was 0.01 V with a scan rate of 50 mV/s and import condition DC setting with N/P polarity.

Results and Discussion

Surface morphology properties

Figure 2 shows the SEM morphologies of the MBI films at different annealing times. At 5 min of annealing time, a valley structure can be observed throughout the surface of MBI, which is due to insufficient heat energy imposed on the MBI film during the annealing process once taken out from the MBI immersion solution. At the same time, the MBI solution disseminated slowly and created a discontinuous solution throughout the TiO_2 film. Consequently, the channelled crack feature upon applied anneal is observed at 5 min of annealing time. As a result, the MBI film revealed a TiO_2 film as can be seen in Figure 2(a), which indicates that TiO_2 peak is almost the same as the MBI peak at 24.58º. In addition, the crystallinity of the MBI film is poor, as confirmed by the XRD result in Figure 4(a). However, the crystallinity of an MBI film starts to improve gradually as the MBI film forms a flat and smooth surface at 10 min of annealing time, as can be seen in Figure 4(b) and Figure 2(b). Interestingly, the MBI peak at 24.58º with low intensity as observed earlier, became higher than TiO_2 peak at 25.37º. It means the surface morphology of MBI film has been improved. As for further increasing the annealing time to 15 min, a little boundary with white colour starts forming as shown in Figure 2(c). On prolonging the annealing time to 20 min, an unclear white boundary, as seen before, became apparent throughout the surface of MBI due to crystallite size increasing gradually, as reported by Ye et al. [18]. This time, a grain boundary appeared and was observed clearly with the white colour of the line on the surface of MBI. As a result, the smooth and flat surface, as seen earlier, became a comparatively rough surface, which might contribute to the crystallite size, which is discussed in Figure 5.

Finally, at 25 min of annealing time, it can be seen clearly that a high density of white grain boundary is observed throughout the MBI surface, yet the MBI films formed do not have a smooth surface. This happened since the application of continuous annealing imposed more heat energy during the longer period of annealing, resulting in a rough surface. It causes the non-smooth and non-flat surface with the seed-grain-like structure to appear dominantly as shown in Figure 2(e). This happened due to the grain growth [8] and crystallization effect [36]. In addition, the reason for the white boundary

increase with increased annealing time is due to the high nucleation rate and growth of micron-sized grains [37] resulting from applying more heat energy into MBI, particularly at the annealing period of 20 min and 25 min. Moreover, the MBI has properties of fast and complete crystallization [38]. In brief, the longer the period of annealing, the clearer increase in the white boundary can be observed, while the shorter the period of annealing, fewer white lines appear instead. Therefore, the appearance of the white boundary depends on the applied annealing period. The uniformness and compactness of an MBI film were further confirmed by cross-sectional SEM images, as shown in Figure 3.

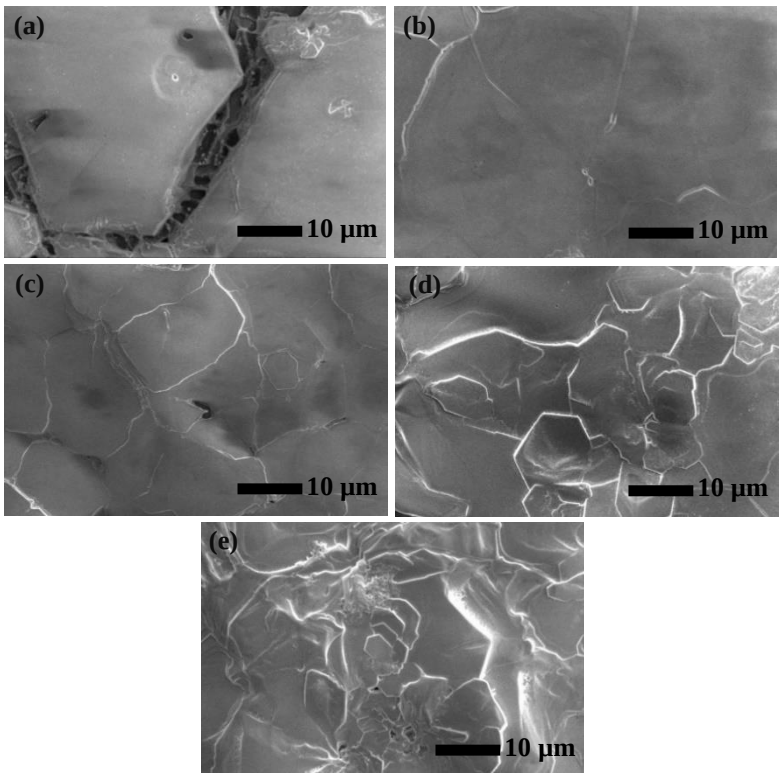

Figure 2: SEM images of MBI films at different annealing times; (a) 5 min, (b) 10 min, (c) 15 min, (d) 20 min, and (e) 25 min

Furthermore, the annealing period, if extended, might influence the strain of a film due to applying heat for a longer time. To validate this, a scientific calculation was performed to confirm the influence of annealing on the microstrain, ε_s, of MBI film by using Equation (1) [45]:

$$\varepsilon_s = \frac{\beta cos\theta}{4} \quad (1)$$

where ε_s is the microstrain of the film, β is the full width at half maximum (FWHM) and θ is the Bragg angle. In brief, the strain is the deformation of the film that experienced the change in structural properties on the application of annealing. The ε_s of MBI film decreased from 0.302 to 0.080 on increasing the annealing period from 5 min to 25 min. It means that the annealing time affects the ε_s of the MBI film due to applied heat on a film at a longer period of annealing. This result is in line with the *D* result which showed an increment that is discussed further in the XRD section.

Cross-sectional SEM images

Figure 3 shows the cross-sectional SEM images of the MBI films at different annealing times. At 5 min, the MBI film was not uniformly formed and discontinuous on the FTO. It can be observed that MBI films formed an island-like structure throughout FTO. As a result, the MBI films are not flat and have non-uniform surfaces. It indicates that the thickness values are far from each other, particularly at 1.633 µm with 0.567 µm, as can be seen in the inset measurement of Figure 4(a), which confirmed that the MBI film was not uniform and not flat surface. On the other hand, Figures 3(b)-(e) show numerous flat, continuous, and smooth MBI films, which confirms that the surface of MBI film is uniform, smooth, and compact. This corresponds to the top-view SEM images in Figures 2(b)-(e). It means that the annealing period of more than 10 min is necessary to obtain a flat, compact, and uniform MBI film by HIM.

In addition, all the thickness values are almost the same in each of the annealing periods after 10 min, for example in 20 min sample, the thickness is 0.554 µm throughout the FTO as shown in Figure 3(d), which further confirmed the MBI film is continuous, uniform, and compact. However, the thickness for the four samples is different, which indicates that the average thickness is 718 nm, 560 nm, 554 nm, and 479 nm for 10 min, 15 min, 20 min, and 25 min, respectively. It means that continuous and uniform films obtained at a longer time are dense and compact having a compressed surface, thereby leading to a decrease in the thickness of the film. Therefore, the period of annealing is a key parameter to control the uniformity and thickness of a film. In brief, at a longer annealing period, more compact, dense, and thinner films were fabricated. However, the shorter annealing period produced non-uniform and thicker films. The film thickness is expected to influence the crystallite size and surface roughness of MBI, which is described in the crystallized size section.

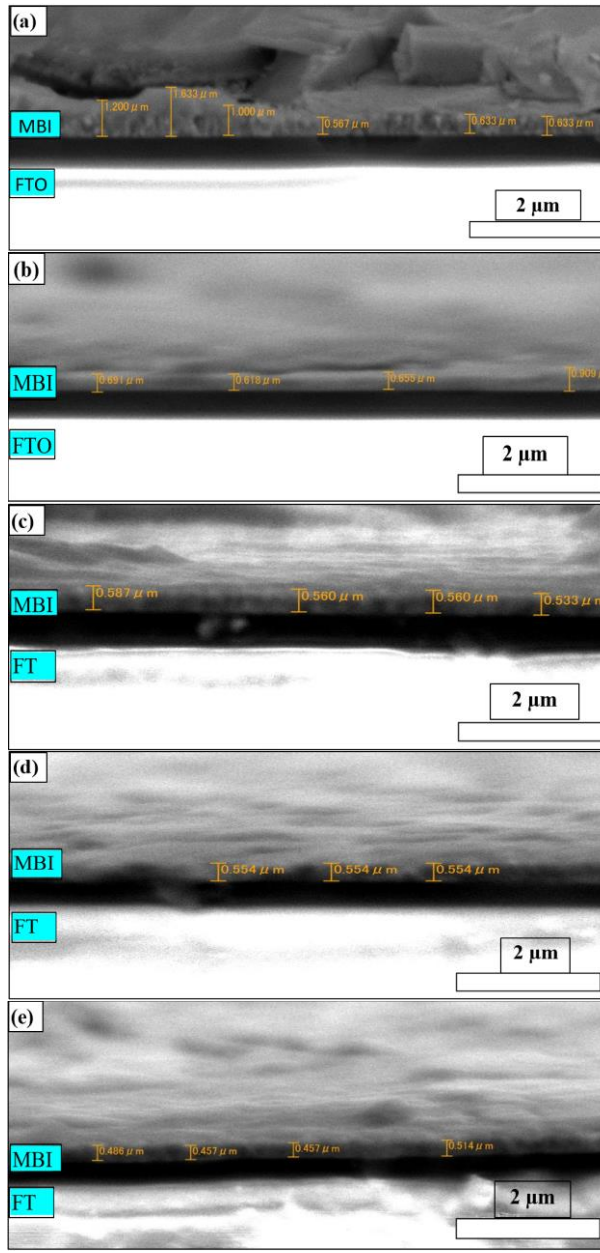

Figure 3: Cross-sectional SEM images of MBI films at different annealing times: (a) 5 min, (b) 10 min, (c) 15 min, (d) 20 min, and (e) 25 min

Structural properties

Figure 4 shows the XRD curves of MBI films annealed at different annealing periods. All the MBI peaks are indexed as hexagonal structures with space group P63/mm using the Joint Committee on Powder Diffraction Standard (JCPDS) card No. 01-070-0666 [34]-[35]. Twelve of the MBI peaks are typically recorded at 11.90°, 12.67°, 14.40°, 16.40°, 17.01°, 24.58°, 29.38°, 32.29°, 41.81°, 42.01°, 43.37°, and 44.71°, which are assigned to the (100), (101), (102), (004), (103), (006), (204), (3-11), (0010), (305), (1010), and (4-12) lattice planes, respectively, and all the peaks are similar to the previous report [30]-[31]. At the earlier phase of the annealing period, 5 min, all the MBI peaks exhibited a low intensity, especially the peak at 24.58° (006), which is almost the same as the TiO_2 peak at 25.37°. The other two peaks of FTO glass can be seen at 26.82° and 38.06°, and one peak of BiOI is recorded at 31.7°, which is due to air exposure during the fabrication of MBI film [7], as shown in Figure 1(a). On increasing the annealing time to 10 min, the MBI peaks slowly increased especially the MBI peak at 16.40° (004) and 24.58° (006). However, on prolonging the annealing period to 15 min, it can be observed that the MBI peak at 24.58° (006) further increases, which is higher than the TiO_2 peak, as compared to earlier seen at 5 min. On further prolonging the annealing time to 20 min, interestingly it can be seen that the MBI peaks at 16.40° (004) and 24.58° (006) further increased, particularly the peak at 24.58° (006), which indicates that the TiO_2 peak at 25.37° further decreases, as shown in Figure 1(d). It means the crystallinity of MBI films improved as the coverage area of MBI on the TiO_2 is enhanced, as shown in SEM images. This happened due to the crystallization effect [36] resulting from imposed heat during the hot immersion under 70 ℃ as the formation of MBI film [30]. Finally, at 25 min of annealing, the MBI peak at 16.40° (004) shows that the crystallinity is further improved, particularly the peak at 24.58° (006) [36]. At the same time, the TiO_2 and BiOI peaks become low in intensity at a longer time of annealing, as can be seen in Figure 1(e). In addition, all the MBI peaks showed narrow and sharp peaks. It means that the MBI films tend to form oxidized bismuth at a longer annealing time, and instead tend to form a high crystalline film with a compact and dense structure, as confirmed by SEM images, which are discussed in the surface properties section. On the other hand, the effect of annealing temperature on the MBI film has been reported in our previously reported work [45]. In brief, by changing the annealing temperature, the grain size of the film is enlarged while the porosity is reduced.

Furthermore, the texture coefficient (TC) was performed to evaluate the effect of P_{pt} on the surface texture of the MBI film and can be calculated according to this equation [46]:

$$TC_{006} = \frac{I_{006} / I^0_{006}}{12^{-1} \sum_{12} I_{hkl} / I^0_{hkl}} \quad (2)$$

where I_{006} and I_{hkl} are the respective measured XRD intensities of the (006) and (*hkl*) planes at the peak height for 12 XRD peaks, and I^o_{006} and I^o_{hkl} are the respective JCPDS powder diffraction intensities of each plane [46]. Using Equation (2), the TC of MBI film increased much from 0.064 to 0.246, by increasing the annealing reaction time from 5 min to 25 min. This increment might be due to the much-changed surface texture of MBI film, which from a uniform and smooth surface, drastically changed to a bigger crystal grain with a rougher surface and white grain boundary evident as shown in Figure 2.

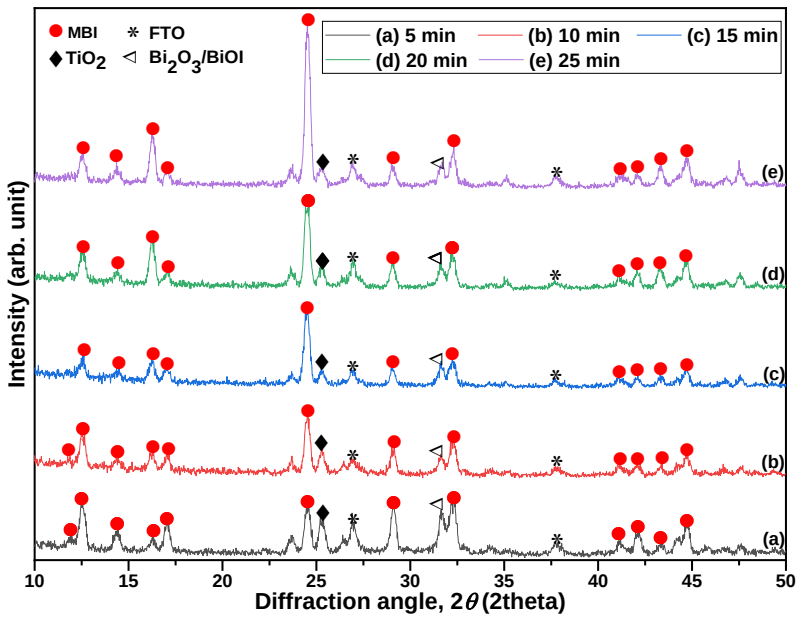

Figure 4: XRD curves of MBI films at different annealing times: (a) 5 min, (b) 10 min, (c) 15 min, (d) 20 min, and (e) 25 min

In addition, the TC result is in line with the result of crystallite size and surface roughness, showing an increment as well, which is further discussed in the next section.

Crystallite size and surface roughness

As discussed earlier in the XRD and SEM section, the crystallinity, compactness, uniformity, and flat surface might influence the crystallite size, *D*, and surface roughness, *Ra*, of an MBI film by increasing the annealing time from 5 min to 25 min as shown in Figure 5.

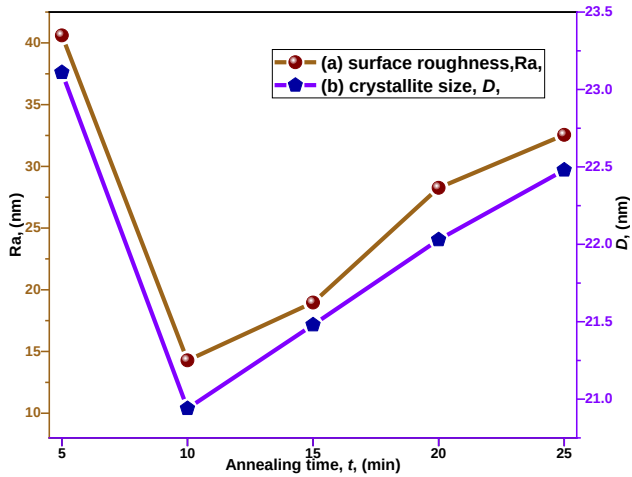

Figure 5: Crystallite size and surface roughness of immersed fabricated MBI films

To confirm that, the measurements of *D* and *Ra* were performed using *Scherrer's* equation [39] and the Dektak measurement, respectively. Figure 5 shows the plotted graph of *Ra* and *D* against the annealing time. It indicates that as the annealing time increases, the trend of increment accordingly is shown by two parameters, except for the sample at 5 min, which might be associated with the cracks present on the surface, as shown in Figure 2(a).

This means that the annealing time influences the *Ra* and *D* of the MBI films. Correspondingly, annealed MBI films at a longer time caused an increase in *D*, which resulted in a rough surface [40]. In brief, in a short time of annealing (10 min), *Ra* and *D* are 14.28 nm and 20.94 nm, respectively. However, at a longer time of annealing (25 min), *Ra* and *D* are 32.55 nm and 22.48 nm, respectively. This means annealed MBI films after a longer period of annealing show crystal grain growth, resulting in a rough surface and large *D* due to the nucleation process [41] and grain growth [8].

UV-vis absorption properties

Figure 6 shows the absorbance spectra of MBI films, and the inset is shown in the *Tauc's* plot for different annealing times. It can be observed that the compact and pinhole-free features of MBI films are attributed to the high absorbance intensity around the visible region as shown in Figures 6(b)-(e), while the cracked feature on the surface of the MBI film (in Figure 2(a)) is attributed to the low absorbance intensity at shorter annealing time as shown in Figure 6(a). In addition, high crystalline and compact films with large *D* and high *Ra*, as can be observed from Figure 5, are attributed to high absorbance, as shown in Figures 6(d)-(e). Xiao et al. [20] reported that the annealing

effectively increased the crystallinity and grain size of perovskite films. As a result, the absorption of light in their perovskite cell was increased. It means that increased crystallinity with increased *D* resulted in fewer low-dimensional defects and less scattering of grain boundaries, which contributed to the high absorbance.

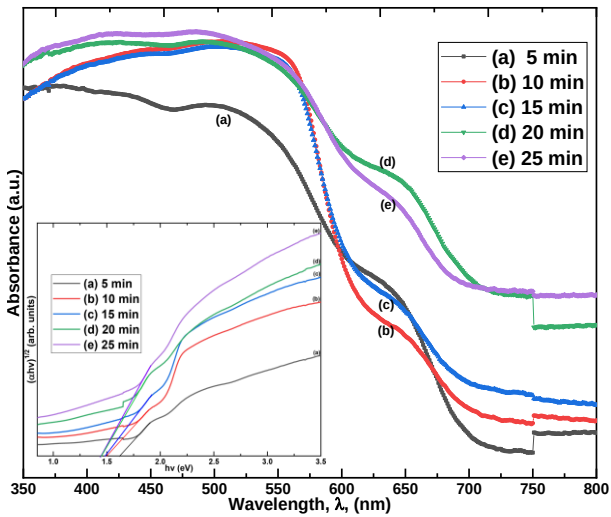

Figure 6: The UV-vis absorption of MBI films at different annealing times: (a) 5 min, (b) 10 min, (c) 15 min, (d) 20 min, and (e) 25 min. *Inset* Tauc's plot of MBI films

Moreover, a shorter annealing time (10 min) found a small *D* and low *Ra*, while a longer annealing time found a large *D* and high *Ra*, as shown in Figure 5. The improved crystallinity of an MBI film resulted in the increase of absorption band-edge up to around 750 nm [21]. Our result agrees well with this finding, where the optical band gap is slightly decreased from 1.63 eV to 1.44 eV, as shown in the inset of Figure 6. This happened due to the films with improved crystallinity, and compact, dense, pinhole-free films, as can be seen in SEM images in Figures 2(d)-(e). Liu et al. [28] reported that the E_g of two-step annealed samples showed a change in the bandgap, which is from 1.58 eV to 1.55 eV due to the improved crystallinity. Our explanation is in line with this finding; however, our recorded value of E_g (1.44 eV) is a little smaller than those reported earlier [28].

Correspondingly, the compact film in our sample contributed to the better absorption of light, which resulted in a better charge trap at the absorber active layer, thereby, producing a high absorbance intensity with the

absorption band-edge shoulder extended to a longer wavelength as shown in Figures 6(d)-(e).

The MBI solar cell performance

Figure 7 shows the I-V curves of fabricated MBI cells at different annealing times, whereas the solar cell parameters are summarized in Table 1.

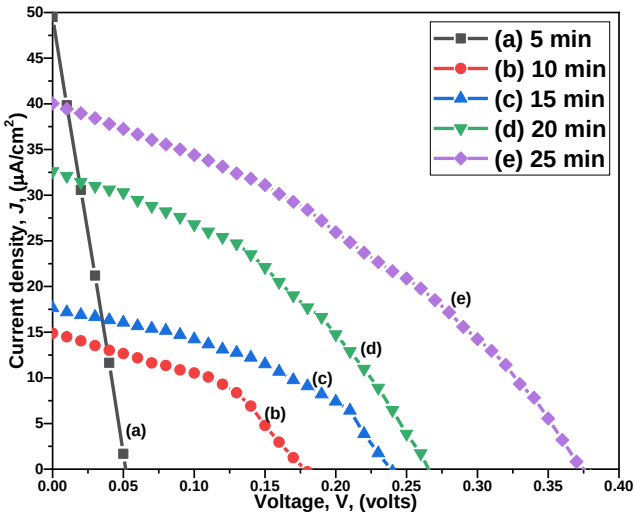

Figure 7: The I-V curves of MBI films at different annealing times: (a) 5 min, (b) 10 min, (c) 15 min, (d) 20 min, and (e) 25 min

It can be observed that at a shorter period of annealing, the short circuit current density and open circuit voltage are low. However, at a longer period of annealing, the current density and voltage are high, except for the sample at 5 min of annealing time. This might be due to the current leakage due to poor morphology as shown in Figure 2(a). Correspondingly, the cracks channelled on the surface of MBI after a shorter annealing period caused the poor extraction of charge carriers and the increase of charge recombination. As a result, the parallel resistance and voltage are low as compared to the other samples, as shown in Figure 7(a). Consequently, the efficiency is extremely low (0.00063%). In contrast with Figures 7(b)-(e) the trend of increment accordingly for both parameters, i.e., short circuit current density (J_{sc}) and open circuit voltage (V_{oc}) is shown in Figures 8(a) and (b), respectively. As a result, the efficiency of the MBI solar cells device shows an increment trend, as indicated in Figure 8(d). This increment is encouraged by a few factors that should be considered. Firstly, the improved morphology and enhanced crystallinity of an MBI film, as discussed earlier in SEM and XRD results,

contribute to the increment of J_{sc} and V_{oc} as shown in Figures 8(a) and 8(b), respectively.

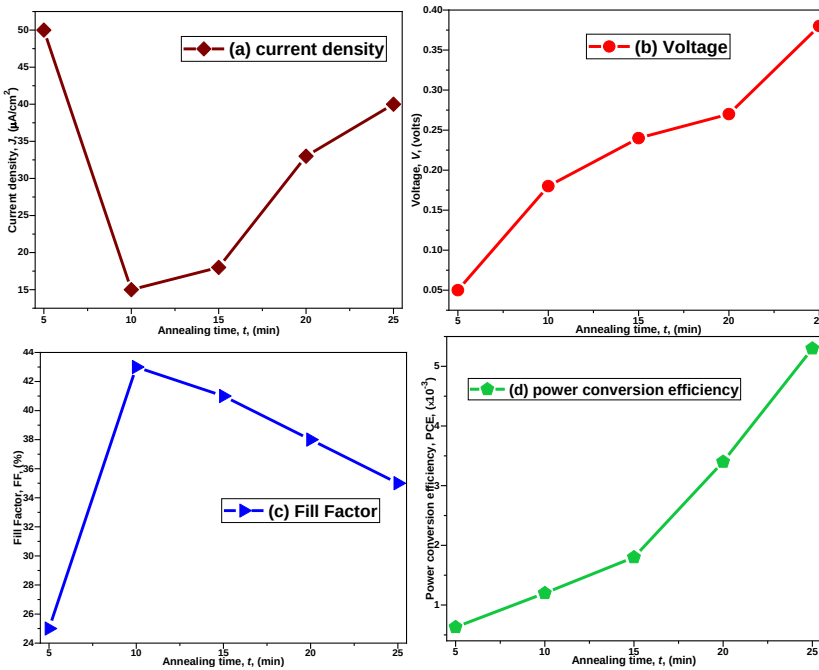

Figure 8: The graph of solar cell parameters of MBI films: (a) current density, (b) output voltage, (c) fill factor, and (d) device efficiency

This happened due to the MBI film being treated with a longer period of annealing causing a compact and high crystallinity film, thus rendering less defect (pinhole-free) on the surface of perovskite film.

In addition, the improved surface morphology can reduce the direct contact between the TiO_2 film and the carbon electrode, as shown in Figure 1. In this case, leakage current and shunting pathway should be inhibited, which reflects the increments of V_{oc} and FF, as indicated in Figures 8(b) and 8(c), respectively. The second factor is the crystallite size, D. The D value showed an increment by increasing the annealing time from 10 min to 25 min, as discussed earlier in the XRD result and shown in Figure 5(b). Consequently, the surface morphology and the crystallinity of MBI films are improved. Thus, the photo-generated carriers are easily collected at the electrode [42], which resulted in an increment of J_{sc}. It means the J_{sc} increases with D values which means a longer period of annealing time creates the large size D, resulting in an increased J_{sc} value because the structural defect density is decreased as

shown in Figures 5 and 8(a). In addition, this increment significantly reduced the charge recombination in the perovskite device, leading to better absorption as discussed earlier in the UV-vis absorption section. Consequently, the MBI cells showed efficient charge extraction from 350 nm to 700 nm in the visible region as shown in the UV-absorbance spectra of the MBI film in Figure 6. Our explanation agrees well with Ran et al. [43] who reported that increasing the *D* might reduce the charge recombination and thus charger can be transported and collected efficiently, thereby improving the performance of the PeSCs device.

Table 1: The solar cell parameters of thickness, crystallite size, and the surface roughness of Bi-PeSCs

Annealing time (min)	J_{sc} ($\mu A/cm^2$)	V_{oc} (volts)	FF (%)	PCE (%)	Ave. *t* (nm)	*D* (nm)	*Ra* (nm)
(a) 5	50	0.05	25	0.0006	944	23.11	40.61
(b) 10	15	0.18	43	0.0012	718	20.94	14.28
(c) 15	18	0.24	41	0.0018	560	21.48	18.96
(d) 20	33	0.27	38	0.0034	554	22.03	28.26
(e) 25	40	0.38	35	0.0053	479	22.48	32.55

Comparison with Previous Studies

Ataei et al. [34], in 2021, fabricated MBI PeSCs by using the spin-coating method, but they suffered a non-uniformity surface morphology of MBI films, and the efficiency of the device was only 0.8%. While Shirahata et al. [44] in 2020, employed the hot air blow technique. The researchers obtained high-quality and rapidly crystallized MBI films; however, the morphology of the films was not uniform; it was rougher and not compact, and the efficiency was only 0.06% [44]. In the same year, Momblona et al. [5] fabricated MBI films through the thermal co-evaporation method and obtained an efficiency of 0.01%; however, the fabricated films were not smooth and had a rougher surface even after employing a complicated process. In 2022, our research group employed multi-step spin-coating and obtained not smooth and compact film with an efficiency of 0.0037% [35]. In brief, all those employed methods still suffered a problem, particularly in terms of film morphology, low efficiency, and a complex fabrication process all of which needed controlling of a few parameters.

Conclusion

The fabrication of MBI cells by using a simple technique of HIM and changing the annealing time was demonstrated for the first time. The annealing time significantly influenced the structural and morphological properties of MBI

films, in which the crystallite size, surface roughness, and thickness were changed, by increasing the annealing time from 5 min to 25 min. SEM images visually depicted the improved morphology with a compact and pinhole-free, while the XRD results exhibited that the crystallinity of MBI is enhanced at 25 min of annealing. As a result, the absorbance increased, and the band-edge absorption was extended towards a longer wavelength. Eventually, the performance of MBI cells showed an eight-fold improvement from 15 μA/cm^2 to 40 μAcm^2. The current study showed that the annealing treatment is effective in improving Bi-PeSCs in the future.

Contributions of Authors

The authors confirm the equal contribution in each part of this work. All authors reviewed and approved the final version of this work. M.F. Achoi: Conducted experimental work, data collecting, and analysis, wrote the original draft, and performed review and editing. S. Kato and N. Kishi: Contribution of ideas and instrumental assistance. T. Soga: Performed supervision, conceptualization, formal analysis, and editing, wrote the review and provided film deposition concept.

Funding

This work received no specific grant from any funding agency.

Conflict of Interests

All authors declare that they have no conflicts of interest

Acknowledgment

The authors would like to acknowledge the Japanese government (MEXT) for the sponsorship throughout this work and unforgettable to the Universiti Teknologi MARA (UiTM) for the study support.

References

[1] Y. Li, J.K. Cooper, R. Buonsanti, C. Giannini, Y. Liu, F.M. Toma, and I. D. Sharp, “Fabrication of planar heterojunction perovskite solar cells by

controlled low-pressure vapor annealing," *Journal of Physcal Chemistry Letters*, vol. 6, no. 3, pp. 493–499, 2015. https://doi.org/10.1021/jz502720a

[2] B. Park, B. Philippe, X. Zhang, H. Rensmo, G. Boschloo, and E.M.J. Johansson, "Bismuth based hybrid perovskites $A_3Bi_2I_9$ (A: Methylammonium or Cesium) for solar cell application", *Advanced Materials*, vol. 27, no. 43. pp. 6806–6813, 2015. https://doi.org/10.1002/adma.201501978

[3] C. Ran, Z. Wu, J. Xi, F. Yuan, H. Dong, T. Lei, X. He, and X. Hou, "Construction of compact methylammonium bismuth iodide film promoting lead-free inverted planar heterojunction organohalide solar cells with open-circuit voltage over 0.8V," *Journal of Physical Chemistry Letters*, vol. 8, no. 2, pp. 394–400, 2017. https://doi.org/10.1021/acs.jpclett.6b02578

[4] S. Sanders, D. Stümmler, P. Pfeiffer, N. Ackermann, G. Simkus, and M. Heuken, "Chemical vapor deposition of organic-inorganic bismuth-based perovskite films for solar cell application", *Scientific Reports*, vol. 9, pp. 1-7, 2019. https://doi.org/10.1038/s41598-019-46199-4

[5] C. Momblona, H. Kanda, A.A. Sutanto, M. Mensi, C. Roldán-Carmona, and M.K. Nazeeruddin, "Co-evaporation as an optimal technique towards compact methylammonium bismuth iodide layers", *Scientific Reports*, vol. 10, p. 10640, 2020. https://doi.org/10.1038/s41598-020-67606-1

[6] R. Nie, A. Mehta, B.W. Park, H.W. Kwon, J. Im, and S.Il. Seok, "Mixed sulfur and iodide-based lead-free perovskite solar cells," *Journal of The American Chemical Society*, vol. 140, no. 3, pp. 872–875, 2018. https://doi.org/10.1021/jacs.7b11332

[7] R.L.Z. Hoye, R.E. Brandt, A. Osherov, V. Stevanovic, S.D. Stranks, M.W.B. Wilson, H. Kim, A.J. Akey, Jo.D. Perkins, R.C. Kurchin, J.R. Poindexter, E.N. Wang, M.G. Bawendi, and V. Bulovic, "Methylammonium bismuth iodide as a lead-free, stable hybrid organic – Inorganic solar absorber," *Chemistry - A European Journal*, vol. 22, no. 8, pp. 2605–2610, 2016. https://doi.org/10.1002/chem.201505055

[8] M. Xiao, F. Huang, W. Huang, Y. Dkhissi, Y. Zhu, J. Etheridge, A. Gray-Weale, U. Bach, Y.B. Cheng, and L. Spiccia, "A fast deposition-crystallization procedure for highly efficient lead iodide perovskite thin-film solar cells", *Angewandte Chemie*, vol. 53, no. 37, pp. 9898–9903, 2014. https://doi.org/10.1002/anie.201405334

[9]. N. Rolston, B.L. Watson, C.D. Bailie, Michael D. McGehee, J.P. Bastos, R. Gehlhaar, J.-E. Kim, D. Vak, A.T. Mallajosyula, G. Gupta, A.D. Mohite, and R.H. Dauskardt, "Mechanical integrity of solution-processed perovskite solar cells", *Extreme Mechanics Letters*, vol. 9, no. 3, pp. 353-358, 2016. https://dx.doi.org/10.1016/j.eml.2016.06.006

[10] J. Feng, "Mechanical properties of hybrid organic-inorganic $CH_3NH_3BX_3$ (B = Sn, Pb; X = Br, I) perovskites for solar cell absorbers",

APL Materials, vol. 2, no. 8, pp. 1-9, 2018. https://doi.org/10.1063/1.4885256

[11] S.M. Jain, D. Phuyal, M.L. Davies, M. Li, B. Philippe, C.D. Castro, Z. Qiu, J. Kim, T. Watson, W.C. Tsoi, O. Karis, H. Rensmo, G. Boschloo, T. Edvinsson, and J. R. Durrant, "An effective approach of vapour assisted morphological tailoring for reducing metal defect sites in lead-free, $(CH_3NH_3)_3Bi_2I_9$ bismuth-based perovskite solar cells for improved performance and long-term stability", *Nano Energy*, vol. 49, pp. 614–624, 2018. https://doi.org/10.1016/j.nanoen.2018.05.003

[12] M.F. Achoi, S. Aiba, S. Kato, N. Kishi, and T. Soga, "Effect of spinning rate on the performance of multilayer bi-perovskite solar cells," *International Journal of Nanoelectronics and Materials*, vol. 14, pp. 1–10, 2021.

[13] B. Conings, L. Baeten, C.D. Dobbelaere, J. D'Haen, J. Manca, and H.G. Boyen, "Perovskite-based hybrid solar cells exceeding 10% efficiency with high reproducibility using a thin film sandwich approach", *Advanced Materials*, vol. 26, no. 13, pp. 2041–2046, 2014. https://doi.org/ 10.1002/adma.201304803

[14] Y. Zhao and K. Zhu, "Solution chemistry engineering toward high-efficiency perovskite solar cells," *Journal Physical Chemistry Letters*, vol. 5, pp. 4175–4186, 2014. https://doi.org/10.1021/jz501983v

[15] T. Singh, A. Kulkarni, M. Ikegami, and T. Miyasaka, "Effect of Electron Transporting Layer on Bismuth-Based Lead-Free Perovskite $(CH_3NH_3)_3Bi_2I_9$ for Photovoltaic Applications", *ACS Applied Materials & Interfaces*, vol. 8, no. 23, pp. 14542–14547, 2016. https://doi.org/10.1021/acsami.6b02843

[16] J. Chen, T. Shi, X. Li, B. Zhou, H. Cao, and Y. Wang, "Origin of the high performance of perovskite solar cells with large grains", *Applied Physics Letters*, vol. 108, no. 5, pp. 053302, 2016. https://doi.org/10.1063/1.4941238

[17] O. Shargaieva,F. Lang, J. Rappich, T. Dittrich, M. Klaus, M. Meixner, C. Genzel, and N.H. Nickel, "The influence of the grain size on the properties of $CH_3NH_3PbI_3$ thin films", *ACS Applied Materials & Interfaces*, vol. 9, no. 44, pp. 38428–38435, 2017. https://doi.org/10.1021/acsami.7b10056

[18] J. Ye, H. Zheng, L. Zhu, X. Zhang, L. Jiang, W. Chen, G. Liu, X. Pan, and S. Dai, "High-temperature shaping perovskite film crystallization for solar cell fast preparation", *Solar Energy Materials and Solar Cells*, vol. 160, pp. 60–66, 2016. https://doi.org/10.1016/j.solmat.2016.10.022

[19] J.-H. Im, I.-H. Jang, N. Pellet, M. Grätzel, and N.-G. Park, "Growth of $CH_3NH_3PbI_3$ cuboids with controlled size for high-efficiency perovskite solar cells", *Nature Nanotechnology*, vol. 9, no. 11, pp. 927–932, 2014. https://doi.org/10.1038/nnano.2014.181

[20] Z. Xiao, Q. Dong, C. Bi, Y. Shao, Y. Yuan, and J. Huang, "Solvent annealing of perovskite‐Induced crystal growth for photovoltaic‐Device efficiency enhancement", *Advanced in Materials,* vol. 26, no. 37, pp. 6503–6509, 2014. https://doi.org/10.1002/adma.201401685

[21] I. Lee, N. Rolston, P. L. Brunner, and R. H. Dauskardt, "Hole-Transport layer molecular weight and doping effects on perovskite solar cell efficiency and mechanical behavior", *ACS Applied Materials & Interfaces*, vol. 11, no. 26, pp. 23757-23764, 2019. https://doi.org/10.1021/acsami.9b05567

[22] T. Mohammad, V. Kumar, and V. Dutta, "Electric field assisted spray coated lead free bismuth iodide perovskite thin film for solar cell application", *Solar Energy,* vol. 182, pp. 72–79, 2019. https://doi.org/10.1016/j.solener.2019.02.034

[23] N.F. Coutinho, S. Cucatti, R.B. Merlo, J.M.C. Silva Filho, N. F. Borrero Villegas, F. Alvarez, A.F. Nogueira, and F. C. Marques, "The thermomechanical properties of thermally evaporated bismuth triiodide thin films", Scientific Reports, vol. 9, pp. 11785, 2019. https://doi.org/10.1038/s41598-019-48194-1

[24] F.X. Xie, D. Zhang, H. Su, X. Ren, K.S. Wong, M. Grätzel, and W.C.H. Choy, "Vacuum-Assisted thermal annealing of $ch_3nh_3pbi_3$ for highly stable and efficient perovskite solar cells", *ACS Nano,* vol. 9, no. 1, pp. 639–646, 2015. https://doi.org/10.1021/nn505978r

[25] H.L. Hsu, C.P. Chen, J.Y. Chang, Y.Y. Yu, and Y.K. Shen, "Two-step thermal annealing improves the morphology of spin-coated films for highly efficient perovskite hybrid photovoltaics", *Nanoscale,* vol. 6, no. 17, pp. 10281–10288, 2014. https://doi.org/10.1039/c4nr02751e

[26] W. Nie, H. Tsai, R. Asadpour, A.J. Neukirch, G. Gupta, J.J. Crochet, M. Chhowalla, S. Tretiak, M.A. Alam, and H. I. Wang, "High-efficiency solution-processed perovskite solar cells with millimeter-scale grains", *Science,* vol. 347, no. 6221, pp. 522–525, 2015. https://10.1126/science.aaa0472

[27] D. Shi, V. Adinolfi, R. Comin, M. Yuan, E. Alarousu, A. Buin, Y. Chen, S. Hoogland, A. Rothenberger, K. Katsiev, Y. Losovyj, X. Zhang, P.A. Dowben, O.F. Mohammed, E.H. Sargent, and O.M. Bakr, "Low trap-state density and long carrier diffusion in organolead trihalide perovskite single crystals", *Science*, vol. 347, no. 6221, pp. 519–522, 2015. https://doi.org/10.1126/science.aaa2725

[28] D. Liu, L. Wu, C. Li, S. Ren, J. Zhang, W. Li, and L. Feng, "Controlling $CH_3NH_3PbI_{3-x}Cl_x$ film morphology with two-step annealing method for efficient hybrid perovskite solar cells", *ACS Applied Materials & Interfaces*, vol. 7, no. 30, pp. 16330–16337, 2015. https://doi.org/10.1021/acsami.5b03324

[29] X. Song, W. Wang, P. Sun, W. Ma, and Z.K. Chen, "Additive to regulate the perovskite crystal film growth in planar heterojunction solar cells",

Applied Physics Letters, vol. 106, no. 3, pp. 033901–033905, 2015. https://doi.org/10.1063/1.4906073

[30] M. F. Achoi, S. Aiba, S. Kato, N. Kishi, and T. Soga, "A novel approach towards compact and improved-crystallinity methylammonium bismuth iodide film via hot immersion method", *Materials Letters: X*, vol. 12, pp. 100096, 2021. doi: https://doi.org/10.1016/j.mlblux. 2021.100096

[31] M. F. Achoi, S. Aiba, S. Kato, N. Kishi, and T. Soga, "Fabrication and properties of compact $(CH_3NH_3)_3Bi_2I_9$ perovskite solar cell by the hot immersion method", *Optical Materials: X*, vol. 15, pp. 1-8, 2022. https://doi.org/10.1016/j.omx.2022.100158

[32] M. F. Achoi, M.A.A. Noman, S. Kato, N. Kishi, and T. Soga, "Synthesis of bismuth triiodide nanofibers by spin-coating at room temperature", *Materialia*, vol. 16, pp. 1-4, 2021. https://doi.org/10.1016/j.mtla.2021 .101077

[33] R.M. Matiur, S. Kato, and T. Soga, "All-solution-processed environment-friendly solid-state BiOI photovoltaic cell with high-short-circuit current by successive ionic layer adsorption and reaction (SILAR)," *Journal of Materials Science: Materials in Electronics*, vol. 32, no. 36, pp. 18342–18350, 2021. https://doi.org/10.1007/s10854-021-06375-7

[34] M. Ataei, M. Adelifard, and S.S. Hosseini, "Physical properties and photovoltaic performance of perovskite solar cells based on lead-free $A_3Bi_2I_9$ (A = CH_3NH_3, Cs) active layers," *Journal of Electronic Materials*, vol. 50, pp. 571–579, 2021. https://doi.org/10.1007/s11664-020-08580-2

[35] M. F. Achoi, S. Aiba, S. Kato, N. Kishi, and T. Soga, "Effect of methylammonium iodide on the all-solution prepared methylammonium bismuth iodide perovskite solar cells performance," *ASM Science Journal*, vol. 17, pp. 1–13, 2022. doi: https://doi.org/10.32802/asmscj.2022.1099

[36] C. Lan, J. Luo, S. Zhao, C. Zhang, W. Liu, S. Hayase, and T. Ma, "Effect of lead-free $(CH_3NH_3)_3Bi_2I_9$ perovskite addition on spectrum absorption and enhanced photovoltaic performance of bismuth triiodide solar cells," *Journal of Alloys and Compounds*, vol. 701, pp. 834–840, 2017. https://doi.org/10.1016/j.jallcom.2017.01.169

[37] H. Feng, C.S. Constantinos, G. Peng, Z. Nanjia, J.M. Tobin, P.H.C. Robert, and G.K. Mercouri, "Solvent-mediated crystallization of $CH_3NH_3SnI_3$ films for heterojunction depleted perovskite solar cells," *Journal of The American Chemical Society*, vol. 137, no. 35, pp. 11455-11452, 2015. https://doi.org/10.1021/jacs.5b06658

[38] S. Oz, J.-C. Hebig, E. Jung, T. Singh, A. Lepcha, S. Olthof, J. Flohre, Y. Gao, R. German, P.H.M.V. Loosdrecht, K. Meerholz, T. Kirchartz, and S. Mathur, "Zero-dimensional $(CH_3NH_3)_3Bi_2I_9$ perovskite for optoelectronic applications", *Solar Energy Materials and Solar Cells*,

vol. 158, no. 2, pp. 195-201, 2016. https://doi.org/10.1016/j.solmat.2016.01.035

[39] M. Dhaouadi, "Physical properties of copper oxide thin films prepared by sol–gel spin–coating method", *American Journal of Physics and Applications*, vol. 6, no. 2, pp. 43-50, 2018. https://doi.org/10.11648/j.ajpa.20180602.13

[40] L. Zhu, J. Shi, S. Lv, Y. Yang, X. Xu, Y. Xu, J. Xiao, H. Wu, Y. Luo, D. Li, and Q. Meng, "Temperature-assisted controlling morphology and charge transport property for highly efficient perovskite solar cells", *Nano Energy*, vol. 15, pp. 540–548, 2015. https://doi.org/10.1016/j.nanoen.2015.04.039

[41] S.S. Shin, J.P. Correa Baena, R.C. Kurchin, A. Polizzotti, J.J. Yoo, S. Wieghold, M.G. Bawendi, and T. Buonassisi, "Solvent-engineering method to deposit compact bismuth-based thin films: Mechanism and application to photovoltaics", *Chemistry of Materials*, vol. 30, no. 2, pp. 336–343, 2018. https://doi.org/10.1021/acs.chemmater.7b03227

[42] H. Feng, C.S. Constantinos, L. Zhao, P.H.C. Robert, and G.K. Mercouri, "Controllable perovskite crystallization at a gas−solid interface for hole conductor-free solar cells with steady power conversion efficiency over 10%," *Journal of The American Chemical Society*, vol. 136, no. 46, pp. 6411–16419, 2014. https://doi.org/10.1021/ja509245x

[43] R. Xiaodong, Y. Zhou, Y. Dong, Z. Xu, C. Dong, L. Yucheng, W. Qingbo, F. Haibo, and L. Shengzhong, "Modulating crystal grain size and optoelectronicproperties of perovskitefilms for solar cells by reaction temperature", *Nanoscale*, vol. 8, no. 6, pp. 816–3822, 2016. https://doi.org/10.1039/c5nr08935b

[44] Y. Shirahata, "Effects of annealing temperature on photovoltaic properties of lead-free $(CH_3NH_3)_3Bi_2I_9$ solar cells," *Journal of The Ceramic Society of Japan*, vol. 128, no. 5, pp. 298–303, 2020. http://doi.org/10.2109/jcersj2.19156

[45] M. F. Achoi, S. Aiba, S. Kato, N. Kishi, and T. Soga, "Influence of post-annealing on the properties of methylammonium bismuth iodide perovsite solar cells through the hot immersion method," *Journal of Electronic Materials*, vol. 52, no. 1, pp. 351-367, 2023. doi: https://doi.org/10.1007/s11664-022-09994-w

[46] Y. Kajikawa, S. Noda, and H. Komiyama, "Preferred orientation of chemical vapor deposited polycrystalline silicon carbide films", *Chemical Vapor Deposition*, vol. 8, no. 3, pp. 99-104, 2022. https://doi.org/10.1002/15213862(20020503)8:3<99::AIDCVDE99>3.0.CO;2-C